

Modulating light with graphene embedded into an optical waveguide

This content has been downloaded from IOPscience. Please scroll down to see the full text.

2014 J. Phys. D: Appl. Phys. 47 335101

(<http://iopscience.iop.org/0022-3727/47/33/335101>)

View [the table of contents for this issue](#), or go to the [journal homepage](#) for more

Download details:

IP Address: 147.91.1.41

This content was downloaded on 21/07/2014 at 10:37

Please note that [terms and conditions apply](#).

Modulating light with graphene embedded into an optical waveguide

Uroš Ralević^{1,2}, Goran Isić¹, Borislav Vasić¹ and Radoš Gajić¹

¹ Center for Solid State Physics and New Materials, Institute of Physics, University of Belgrade, Pregrevica 118, 11080 Belgrade, Serbia

² Faculty of Electrical Engineering, University of Belgrade, Bulevar Kralja Aleksandra 73b, PO Box 35-54, 11120 Belgrade, Serbia

E-mail: uros@ipb.ac.rs

Received 27 April 2014, revised 11 June 2014

Accepted for publication 23 June 2014

Published 18 July 2014

Abstract

We investigate the influence that an embedded graphene layer has on guided modes of optical waveguides using exact numerical calculations and a convenient perturbation theory. The latter is found to be highly accurate allowing the graphene-induced changes of modal propagation constants to be determined as the product of a numerical factor characterizing the modal properties of the bare waveguide and the optical conductivity of graphene. In this manner, the influence of the waveguide geometry and the electro-optical properties of graphene on the modulation efficiency can be considered and optimized separately. This result is then used to illustrate the basic electro-absorptive and electro-refractive modulator design principles on a planar waveguide toy model with realistic parameters.

Keywords: waveguides, graphene, electro-optical modulators

(Some figures may appear in colour only in the online journal)

1. Introduction

The electrical [1] and optical [2] properties of graphene, the two-dimensional allotrope of carbon, have attracted considerable interest in the past few years. In spite of being only one atom thick, a single free-standing sheet of graphene will, upon illumination, absorb around [3] $\pi\alpha \approx 2.3\%$ of the incoming light regardless of its frequency. Such a significant (per atom) and spectrally flat absorbance is a consequence of graphene's peculiar electronic structure and is implied by the honeycomb arrangement of carbon atoms [4].

The crucial property that makes graphene a promising material for optoelectronics is the so-called electric field effect [1]. It allows the electron (or hole) concentration, and consequently the optical conductance $\sigma(\omega)$, to be tuned via electrical gating [2], thus establishing graphene as the ultimate electro-optic material. The ensuing gate-controlled absorption and its compatibility with standard CMOS and SOI technologies indicate that graphene has a high potential as a building block of various optoelectronic devices [5–7] including photodetectors [8, 9], optical modulators [10, 11], polarizers [12, 13], sensors [14] and mode-locked lasers [15].

We consider a generic type of graphene-based electro-optical modulators characterized by graphene being embedded into an optical waveguide. The recent surge of interest [10, 11, 16–20] in such systems is motivated by the fact that highly localized photons of the waveguide can interact very efficiently with graphene. The augmented photon–graphene interaction is a consequence of the enhanced optical density of states in the waveguide.

While $\sigma(\omega)$ depends on doping, as quantified by the Fermi energy E_F , for values of E_F achievable in practice [2], graphene behaves invariably as a weak conductor. Therefore, upon insertion into the waveguide, a graphene layer will only weakly perturb the fields of a given mode by inducing a slight change in its propagation constant. So far, most attention has been devoted to structures in which modulation is based on the graphene-induced change in the imaginary part of the propagation constant [10, 11, 16–23]. Since it means that light is absorbed as it propagates along the waveguide, the ensuing devices are referred to as electro-absorptive modulators (EAM). Alternatively, in electro-refractive modulators (ERM) light is modulated in a Mach–Zehnder setup [24, 25], using graphene to tune the real part of the propagation constant of light in one of the arms. In either case, recent work [10, 11, 18]

has shown that optical modulators based on waveguides coupled with graphene are already comparable to, if not better than, traditional semiconductor optical modulators (Si, GeSi and InGaAs) [26, 27] in terms of a broad optical bandwidth, small device footprint, high operation speed, large modulation depth (MD) and small insertion losses (ILs).

This paper addresses the problem of understanding the effect that graphene has on guided modes of a waveguide at telecommunication (near-infrared) frequencies. The existing studies mentioned above, experimental or theoretical, report on characteristics of particular waveguide geometries leaving aside questions on how would the device performance change by varying any of the geometrical or material parameters. Here we introduce a method that can predict the effect of parametric variations, which is essential in the design of graphene-based modulators. The method is based on perturbation theory [28, 29] that treats graphene as a perturbation to the waveguide in which it is embedded, henceforth referred to as the bare waveguide. Using planar waveguides as a toy model, we show that perturbation theory is virtually exact for a wide range of realistic material parameters. We show that the change in the propagation constant induced by graphene equals the product of a numerical factor $G(\omega)$, quantifying the modal properties of the bare waveguide, and the optical conductance of graphene $\sigma(\omega)$. We then proceed with the toy model to show how this fact can be used to facilitate the understanding and design of graphene-based modulators.

2. Model and theory

2.1. Model

A planar dielectric waveguide extending infinitely along the y and z directions is illustrated in the inset of figure 1. We consider this simple geometry as a toy model, while it will be evident that the reasoning is straightforwardly extended onto waveguide geometries used in practice, such as the ridge (silicon bus) waveguide [10, 11] or an optical fibre [12]. The thickness of the waveguide (layer 2) is d while the superstrate (layer 1) and substrate (layer 3) are semi-infinite in the x direction. Light waves are assumed to propagate in the y direction, their propagation constant being denoted by k_y .

We shall consider the typical case of $\epsilon_2 > \epsilon_3 > \epsilon_1$, corresponding to a waveguiding slab of permittivity ϵ_2 grown on a substrate with permittivity ϵ_3 and surrounded by air with $\epsilon_1 = 1$. In particular, we shall consider the technologically most relevant case of a silicon-on-insulator (SOI) system where the waveguide is made of silicon with a silicon-dioxide substrate. Around the telecommunication frequencies ($\lambda \approx 1.5 \mu\text{m}$), the silicon and silicon-dioxide permittivities are [30] $\epsilon_2 = 12.25$ and $\epsilon_3 = 2.25$.

The electromagnetic fields in the waveguide are classified into transverse electric (TE) and transverse magnetic (TM) modes. By TE (TM) we designate modes having the electric (magnetic) field vector parallel to z . The graphene layer indicated by the dashed line in the inset of figure 1 is positioned at distance h from the left end of the slab, and modelled as an infinitely thin layer with surface conductivity $\sigma(\omega)$ [31].

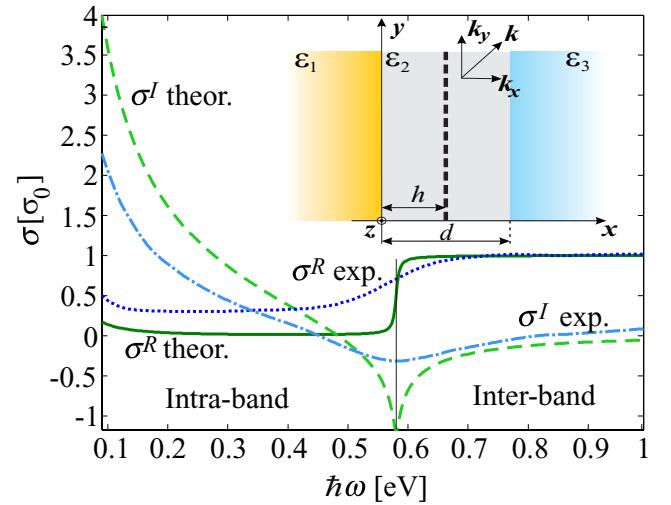


Figure 1. Real σ^R (solid line) and imaginary σ^I (dashed line) part of graphene's optical conductivity obtained from equations (1) and (2) for $E_F = 0.29$ eV, $\tau = 1.77 \times 10^{-13}$ s and $T = 45$ K. The experimental σ^R (dotted line) and σ^I (dashed-dotted line) curves are taken from [2] for $V = 71$ V, corresponding to $E_F \approx 0.29$ eV. Inset shows the illustration of the planar waveguide geometry with graphene (the vertical dashed line) positioned at distance h from the waveguide–superstrate interface.

The conductivity $\sigma(\omega)$ comprises two contributions originating from inter-band and intra-band transition processes, i.e. $\sigma(\omega) = \sigma_{\text{inter}}(\omega) + \sigma_{\text{intra}}(\omega)$, these terms being given by [31]

$$\sigma(\omega)_{\text{inter}} \approx \frac{iq^2}{4\pi\hbar} \ln \left(\frac{2E_F - \hbar(\omega + i/\tau)}{2E_F + \hbar(\omega + i/\tau)} \right), \quad (1)$$

and

$$\sigma(\omega)_{\text{intra}} = \frac{iq^2 k_B T}{\pi \hbar^2 (\omega + i/\tau)} \times \left[\frac{E_F}{k_B T} + 2 \ln \left(\exp \left(\frac{-E_F}{k_B T} \right) + 1 \right) \right]. \quad (2)$$

Here τ and T denote the electron relaxation rate and temperature, respectively. The elementary charge is denoted with q . For low frequencies ω , such that $\hbar\omega \ll 2E_F$, the intra-band (Drude-like) term of the conductivity dominates. At high frequencies, $\hbar\omega \gg 2E_F$, the σ_{intra} term is negligible while σ_{inter} approaches the universal optical conductance [3] $\sigma_0 = q^2/4\hbar$. As we study the influence that changing of E_F has on waveguide modes and as this is effected via the change in $\sigma(\omega)$ with E_F , it is useful to bear in mind that all the $\sigma(\omega)$ spectra with different E_F are similar, each having the characteristic features (minima of the imaginary and a step in the real part) centred at $\hbar\omega = 2E_F$, see figure 1.

While values of $\sigma(\omega)$ given by equations (1) and (2) are widely used in the literature, it should be noted that they represent an idealized case that describes graphene only qualitatively, since they are derived by neglecting the temperature and frequency dependence of τ . To show this, in figure 1 we plot the theoretical $\sigma(\omega)$ calculated from equations (1) and (2) along with $\sigma(\omega)$ values that have been measured in [2] under idealistic conditions (high-quality exfoliated graphene measured in vacuum at $T = 45$ K). Here and henceforth, σ^R and σ^I denote the real and imaginary

component of $\sigma(\omega)$, respectively. The experimental curves, denoted as ‘exp.’ in figure 1, represent the 71 V (highest voltage) case from [2] corresponding to $E_F \approx 0.29$ eV. The theoretical curves (‘theor.’) are drawn by taking $\tau = 1.77 \times 10^{-13}$ s, which is estimated as the intra-band relaxation time in [2] for the 71 V case, and $T = 45$ K. Despite the fact that $T = 45$ K is taken to match the experimental data in [2], it should be noted that equations (1) and (2) predict small, practically negligible, temperature dependence of the conductivity in the range of frequencies used in this work. For the sake of simplicity, these values of τ and T are used throughout the paper whenever $\sigma(\omega)$ is calculated from equations (1) and (2). The comparison in figure 1 shows a marked difference between the two datasets with theoretical curves being much sharper. Moreover, the parameters of wafer-scale graphene produced either epitaxially [32] or by chemical vapour deposition [33] and used under ambient conditions are likely to be even more flattened-out. Below we show that the method developed in this paper is ideally suited for easily assessing the effect that realistic spectra of $\sigma(\omega)$ would have on a modulator.

A waveguide mode of the figure 1 geometry with frequency ω and propagation constant k_y comprises plane-wave components in the three layers, each satisfying the following dispersion relation [34]

$$k_n^2 = \epsilon_n \epsilon_0 \mu_0 \omega^2 - k_y^2, \quad (3)$$

where k_n is the x -component of the wave vector \mathbf{k} , and $n = 1, 2, 3$ denotes layers of the structure. In case of a lossless waveguide, guided modes have a real propagation constant k_y , with k_n being purely imaginary in layers 1 and 3 and purely real in the slab. The inclusion of graphene induces losses and the propagation constant becomes complex i.e. $k_y = k_y^R + ik_y^I$. Accordingly, the value of k_n becomes complex in all three layers. For guided modes of a waveguide coupled with graphene, the complex k_y at a particular frequency ω can be numerically determined from the complex reflection coefficient using the reflection pole method [35, 36]. For both TE and TM modes, the complex reflection coefficient is obtained by the standard transfer matrix formalism.

As an example, figure 2 shows the dispersion curves of the two lowest TE and TM (fundamental and first-order) modes calculated by the outlined numerical procedure. The thickness of the silicon ($\epsilon_2 = 12.25$) slab was set to $d = 220$ nm while silicon-dioxide ($\epsilon_3 = 2.25$) is assumed as the substrate. The graphene layer is assumed to be placed in the centre of the slab, $h = d/2$, with $\sigma(\omega)$ calculated from equations (1) and (2) with $E_F = 0.4$ eV. Solid lines show the real, k_y^R (left panels), and imaginary, k_y^I (right panels), dispersions of the fundamental TE (figures 2(a) and 2(b)) and TM (figures 2(c) and 2(d)) modes, while dashed lines represent the first-order TE and TM modes. Insets of figure 2 depict the corresponding field distributions for TE and TM modes at frequency $\hbar\omega = 1.45$ eV.

Since the waveguide is asymmetric, all modes, regardless of being TE or TM polarized, have a cut-off frequency. The modes of the bare waveguide are not depicted: the dispersion of k_y^R would practically overlap the graphene-coupled dispersions, while the k_y^I components are identically

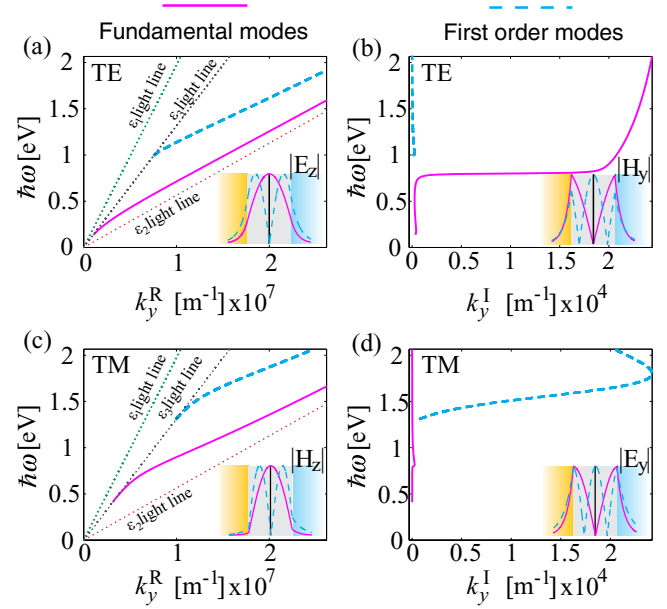


Figure 2. Calculated real $k_y^R(\omega)$ and imaginary $k_y^I(\omega)$ dispersion curves for a $d = 220$ nm thick SOI waveguide, $\epsilon_1 = 1$, $\epsilon_2 = 12.25$, $\epsilon_3 = 2.25$ and assuming the theoretical $\sigma(\omega)$ calculated for $E_F = 0.4$ eV. (a) and (b) show the real and imaginary parts of k_y for the fundamental and the first-order TE modes, while (c) and (d) depict the two lowest TM modes. The insets depict the modal field distributions at $\hbar\omega = 1.45$ eV.

equal to zero in the bare waveguide. Also, the field distributions of a graphene-coupled waveguide are practically the same as those of the bare waveguide. Therefore, the effect of graphene is to introduce nonzero values of k_y^I and to slightly shift k_y^R (not visible in the current scale). Here the cut-offs of the fundamental TE and TM modes of the bare waveguide are at 0.1 eV and 0.38 eV, while the graphene coupled waveguide cut-offs are slightly blueshifted to 0.11 eV and 0.39 eV, respectively.

2.2. Perturbation theory

Since the coupling of a graphene layer with the waveguide induces small changes in the propagation constant of a waveguide mode, one can treat graphene as a perturbation to the bare waveguide and apply a perturbation technique to evaluate those changes. Following [28, 29], for a given mode with fields \mathbf{E} and \mathbf{H} of the bare waveguide, a change in the mode's propagation constant Δk_y at frequency ω can be expressed as

$$\Delta k_y = i\sigma(\omega) \frac{|E_{\parallel}(h)|^2}{4P}, \quad (4)$$

where $P = 1/2 \int (\mathbf{E} \times \mathbf{H}^*) \cdot \mathbf{y} dx$ is the time-averaged power flux per unit length along the z direction in the bare waveguide and E_{\parallel} represents the bare mode electric field component parallel with the graphene layer: $E_{\parallel} = E_z$ for TE modes and $E_{\parallel} = E_y$ for TM modes. Introducing U as the modal electromagnetic energy per unit length along y and z , which is well defined in the lossless waveguide [37], $U = 1/4 \int (\epsilon \epsilon_0 |\mathbf{E}|^2 + \mu \mu_0 |\mathbf{H}|^2) dx$, and the modal group velocity of the bare waveguide, $v_g = d\omega/dk_y$, equation (4)

becomes [29]

$$\Delta k_y = i\sigma(\omega)G(\omega, h), \quad (5)$$

where

$$G(\omega, h) = \frac{|E_{||}(h)|^2}{4v_g U}. \quad (6)$$

If U is set to unity, i.e. the in-plane electric field is normalized to the total energy in the waveguide, equation (6) is simplified to

$$G(\omega, h) = \frac{|e_{||}(h)|^2}{4v_g}, \quad (7)$$

where $e_{||}$ denotes the normalized in-plane electric field of the unperturbed waveguide.

As σ is a complex quantity, i.e. $\sigma = \sigma^R + i\sigma^I$, it becomes clear that

$$\Delta k_y^R = -\sigma^I(\omega)G(\omega, h), \quad \Delta k_y^I = \sigma^R(\omega)G(\omega, h). \quad (8)$$

Equation (8) is the main result of this section. It indicates that, if graphene only weakly perturbs the waveguide modes, the changes in the real and imaginary parts of the propagation constant are directly determined as a product of $G(\omega, h)$, which is an inherent property of the bare waveguide, and the imaginary and real parts of $\sigma(\omega)$, respectively. Furthermore, separation of graphene and the waveguide provided by the perturbation method significantly simplifies numerical calculations. Below we show, by comparing the predictions of equation (8) with exact values calculated by the reflection pole method, that the perturbation method is very accurate and demonstrate the advantages of using equation (8) in discussing graphene-coupled waveguides.

3. Accuracy of perturbative expressions

To test the validity of equation (8), we consider the SOI waveguide from figure 2. We calculate $\Delta k_y = \Delta k_y^R + i\Delta k_y^I$ by the reflection pole method ('Exact') and compare the results with the perturbative values ('Perturbation method'), for two values of E_F . Figure 3 shows the comparison of Δk_y^R and Δk_y^I for the fundamental TE, panels (a) and (b), and TM mode, panels (c) and (d). Since both the imaginary and real parts of the conductivity change with E_F , the cut-offs for the two investigated values of E_F will slightly differ. For example, when the Fermi level is $E_F = 0.29$ eV, the cut-off of the fundamental TE mode is 0.105 eV, while for $E_F = 0.4$ eV and $E_F = 0.7$ eV the cut-offs rise to 0.11 eV and to 0.115 eV, respectively. A similar, though much smaller, shift is found for the TM mode cut-off. The comparisons in figure 3 are plotted from the higher cut-off of the corresponding mode. We find that the agreement between the perturbative and exact curves is excellent.

The values of $|\Delta k_y|$ for the TE mode, shown in figures 3(a) and (b), are around two orders of magnitude larger than the corresponding values of the TM mode in figures 3(c) and (d). To explain the origin of this difference and show how Δk_y depends on where graphene is placed within the waveguide, the $G(\omega, h)$ factor is plotted as a function of the spatial coordinate $x = h$ and frequency $\hbar\omega$, for both TE (figure 4(a)) and TM

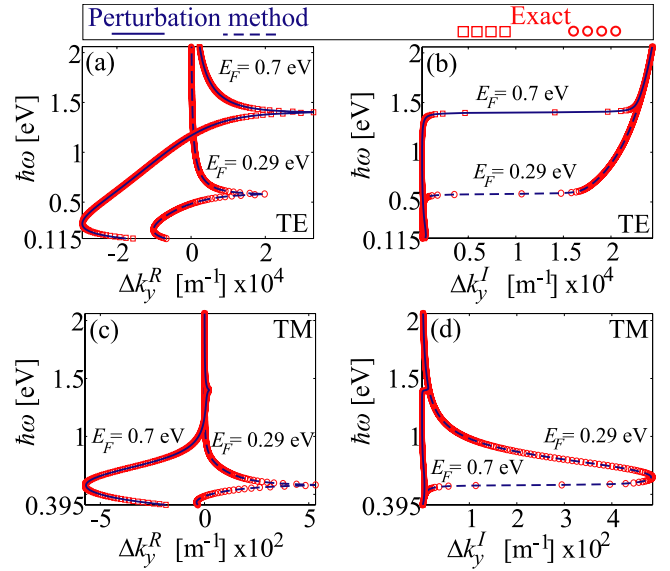


Figure 3. Comparison of the numerically calculated ('Exact') and the perturbative ('Perturbation method') values of the graphene-induced changes of the propagation constant Δk_y , obtained for the waveguide from figure 2. The top row, (a) and (b), shows the real and imaginary parts of Δk_y for the fundamental TE mode, while the bottom row, (c) and (d), shows the corresponding quantities for the TM mode.

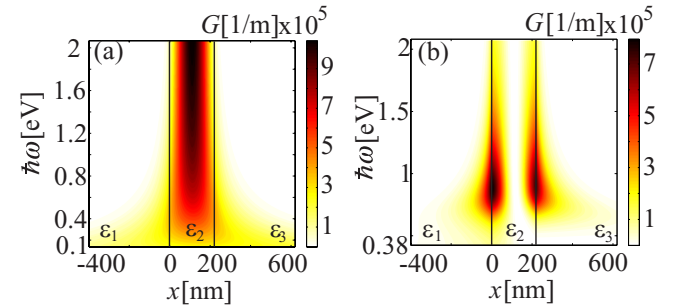


Figure 4. The G -factor of (a) the fundamental TE and (b) the fundamental TM mode for the SOI waveguide given in figure 2, plotted as a function of both the frequency ω and the position of graphene, $h = x$.

(figure 4(b)) modes. Here, the G is divided by the vacuum impedance $z_0 = \sqrt{\mu_0/\epsilon_0}$ and plotted in units of m^{-1} .

The spatial distribution of $G(\omega, h)$ at frequency ω represents the spatial distribution of the normalized in-plane electric field at that frequency divided by the modal group velocity. The obvious outcome of equation (8) is thus the well-known fact that a mode couples more strongly to graphene when the position of the graphene layer h is set to points of the in-plane electric field maxima. The much larger $|\Delta k_y|$ of the fundamental TE mode than the TM mode values is evidently the consequence of setting $h = d/2$ in calculations for figure 3. However, the more important outcome of equation (8) is that it allows a direct comparison of coupling strengths at different frequencies and waveguide geometries, simply by comparing $G(\omega, h)$.

As the frequency increases, both TE and TM modes in figure 4 become more confined to the slab. In symmetrical waveguides, the field amplitude minima (nodes) and maxima

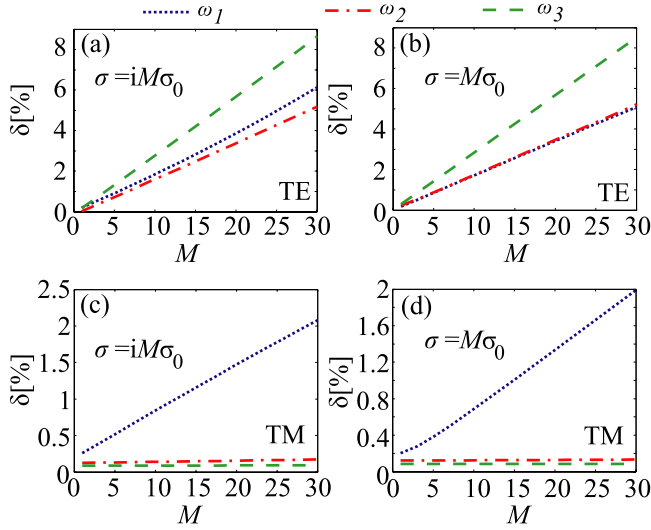


Figure 5. Relative errors δ as a function of σ for purely imaginary values, (a), (c), and purely real values, (b), (d). The top panels show δ for the fundamental TE mode of the SOI waveguide from figure 2 calculated at $\hbar\omega_1 = 0.35$ eV, $\hbar\omega_2 = 1.1$ eV and $\hbar\omega_3 = 1.85$ eV. The bottom panels show the corresponding δ for the fundamental TM mode, calculated at $\hbar\omega_1 = 0.55$ eV, $\hbar\omega_2 = 1.2$ eV and $\hbar\omega_3 = 1.9$ eV.

(antinodes) have fixed positions determined by symmetry. Here, due to the substrate–superstrate asymmetry, the normalized field minima and maxima shift with ω approaching the middle of the slab with increasing ω . At lower frequencies, especially near the cut-offs, these extremal points are slightly shifted towards the substrate. Thus, by positioning graphene $h = d/2$, the coupling efficiency is nearly maximized (minimized) for the TE (TM) mode for frequencies sufficiently above the cut-off.

Having seen that the perturbative expression appears highly accurate for single-layer graphene, we now attempt to quantify this accuracy and establish the limits of its validity. To this end, we introduce the relative error as $\delta = |\Delta k_y^e - \Delta k_y^p| / |\Delta k_y^p|$, with ‘e’ and ‘p’ indicating the exact and perturbative values, respectively. The extent to which graphene will perturb a mode of a given frequency ω is clearly determined by how big $\sigma(\omega)$ is which, in turn, depends on E_F . In the range of telecommunication frequencies ($\lambda \approx 1.5 \mu\text{m}$) relevant for this study, the practically achievable [2] values of E_F are such that $|\sigma(\omega)|$ is a few σ_0 at most. Therefore, in figure 5 we investigate δ by selecting a mode of a given frequency and polarization and then calculate the variation of δ as a function of the real or imaginary parts of $\sigma(\omega)$.

The calculations shown in figure 5(a) are made for the fundamental TE mode of the SOI structure described in figure 2 where the conductivity of graphene is swept over purely imaginary values, $\sigma = iM\sigma_0$, M being a real number varied between 0 and 30. The curves are drawn for three frequency values, ω_1 being close to the cut-off (dotted), ω_2 being in the middle of the investigated range (dashed–dotted) and ω_3 being at the higher end of the investigated spectral interval, see figure 5. For panel (b), we repeated the calculations but by sweeping σ over purely real values, $\sigma = M\sigma_0$. The same procedure carried out for the fundamental TM mode results in plots shown in figures 5(c) and (d).

All of the relative errors shown in figure 5 are below 9% up to above $M = 30$ and almost independent of whether σ is real or imaginary. The reason that δ increases with M is that the field distributions of the perturbed waveguide gradually become more different from those of the bare waveguide, meaning that the assumptions made in deriving the perturbative expressions [28, 29] gradually break down. Considering that the values of $|\sigma(\omega)|$ are expected to be $\sim 3\sigma_0$ – $4\sigma_0$ at most, see figure 1(b), $M = 30$ would correspond to inserting around 10 layers of graphene into the waveguide, which is much more than the technologically relevant case of one or two layers [10, 11]. Therefore, figure 5 asserts that the expected worst-case accuracy of the perturbative expressions for a single graphene layer is better than 1% and that it is well behaved even for a larger number of layers. The relative errors found in panels (c) and (d) are lower simply because here the placing of graphene is such that it weakly interacts with the TM mode. Clearly, the G factor also determines the accuracy of perturbative expressions since high values of G lead to a stronger interaction of the mode’s field and the graphene. But, as long as the condition of a small perturbation is met this approach can be applied to any type of waveguides, for example slot waveguides, with accuracy better than a few per cent. Specially, for plasmonic waveguides one needs to consider complex mode frequencies and adjust the perturbation technique accordingly.

4. Graphene-based optical modulators

In section 1, we mentioned that there are two strategies in designing graphene-based optical modulators. In more popular EAMs, graphene is used for tuning the absorption of the wave as it propagates along the waveguide. The efficiency of such a modulator is, therefore, determined from the graphene-induced variation of Δk_y^I . Alternatively, in ERM [24, 25] graphene is used to induce a phase shift meaning that the efficiency of ERM is determined by the magnitude of Δk_y^R . In view of equation (8), we find that in both cases, the efficiency of the modulation is proportional to the $G(\omega)$ factor. Therefore, the starting point of the design of a graphene-based modulator is finding a waveguide geometry that will have a maximum value of $G(\omega)$ for the frequency and optical mode at which the modulator is operated.

Here we limit our consideration to the fundamental TE mode and investigate how the change in the waveguide permittivity ε_2 and thickness d affect $G(\omega)$, assuming that the superstrate and substrate permittivities are kept fixed at $\varepsilon_1 = 1$ and $\varepsilon_3 = 2.25$, respectively. As explained before, the optimum position of graphene is in the vicinity of the middle of the waveguiding slab, so we fix $h = d/2$. For highly confined fields this configuration yields at least four times greater modulation efficiency than the one achievable with configurations in which graphene is positioned on the edges of the slab (see figure 4(a)). Configurations having a nanostructure embedded in the middle of the waveguide, similar to the one we chose to analyse, have already been experimentally demonstrated [38].

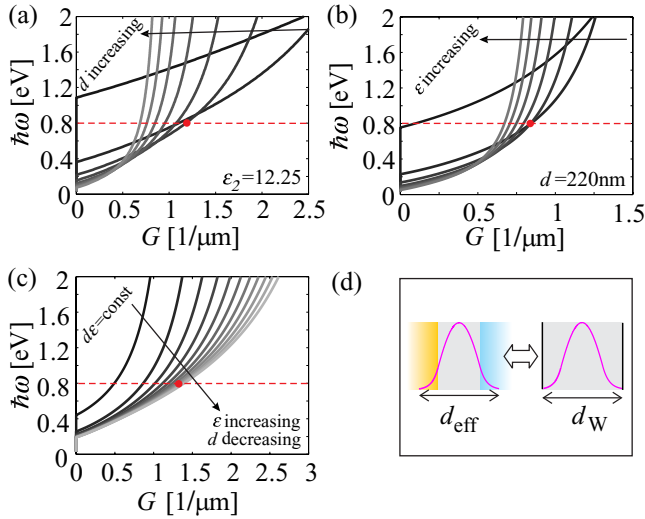


Figure 6. Parametric analysis of $G(\omega)$ at $h = d/2$ and assuming air ($\epsilon_1 = 1$) and silicon-dioxide ($\epsilon_3 = 2.25$) as the superstrate and substrate, respectively. In (a) the waveguide thickness d is varied, while ϵ_2 is fixed; in (b) the thickness is fixed while ϵ_2 is varied. In (c) both d and ϵ_2 are varied but their product is constant. The horizontal (red) dashed lines indicate the assumed operating frequency, $\hbar\omega = 0.8$ eV, while the dot denotes the intersection with the $G(\omega)$ curve that gives the maximum G -factor. (d) Illustration of the analogy between the investigated SOI waveguide and a fictive PEC waveguide.

Figure 6(a) depicts the variation of $G(\omega)$ with fixed $\epsilon_2 = 12.25$ and with the waveguide width d varied. The frequencies at which the various $G(\omega)$ curves reach zero are the corresponding cut-offs. As d is swept from 20 to 300 nm in steps of 40 nm, the cut-off is seen to decrease from around $\hbar\omega = 1.1$ eV to below $\hbar\omega = 0.1$ eV. Assuming that a modulator operating at $\hbar\omega = 0.8$ eV is sought, we find that the optimal thickness is around $d = 100$ nm, as indicated by the intersection of the (red) dashed line with the $G(\omega)$ curve.

Alternatively, in figure 6(b) we show the variation of $G(\omega)$ when ϵ_2 is varied between 3.25 and 21.25 in steps of 3, assuming $d = 220$ nm is fixed. The cut-offs are seen to redshift with increasing ϵ_2 , as the optical width $\sqrt{\epsilon_2}d$ of the slab is being increased. Amongst the plotted curves, two corresponding to $\epsilon_2 = 6.25$ and $\epsilon_2 = 9.25$ are found to have the largest value of $G(\omega)$ at $\hbar\omega = 0.8$ eV, indicating again that the optimal value of ϵ_2 lies between these two values.

A common characteristic of the $G(\omega)$ curves shown in figures 6(a) and (b) is that they start from $G = 0$ at the cut-off and steadily increase gradually saturating at high frequencies. Here we are interested in the near-infrared spectral region, so the curves are not plotted up to the saturation frequencies. The effective mode width, d_{eff} , defined as the width within which the fields of the guided mode fall sufficiently close to zero, is infinite at the cut-off (the mode is not confined) and gradually decreases with increasing ω . The saturation of $G(\omega)$ occurs because d_{eff} saturates with increasing ω , as the mode becomes tightly confined to the slab. Therefore, the shape of $G(\omega)$ simply reflects the fact that the fields become more confined at higher ω . The dependence of the limiting value at which $G(\omega)$ saturates on d_2 and ϵ_2 can be understood

in analogy with a waveguide having a perfectly conducting cladding (PEC waveguide), as depicted in figure 6(d). For frequencies sufficiently above the cut-off, the group velocity of the fundamental TEM mode of the PEC waveguide can be considered constant and $G(\omega)$ is found to be proportional to $1/(d_W \epsilon_W)$, d_W and ϵ_W denoting its thickness and permittivity. Therefore, waveguides having small values of the $\epsilon_2 d$ product are expected to give larger values of $G(\omega) \sim 1/\epsilon_2 d$ at high frequencies but at a given operating frequency that will be counterbalanced by the vicinity of the cut-off frequency which is, to the first approximation, proportional to $1/\sqrt{\epsilon_2}d$. In other words, the optimal geometry for a given operating frequency is found as a trade-off between high confinement and a sufficiently low cut-off frequency.

A further insight into the dependence of $G(\omega)$ on the geometry is found by studying figure 6(c) where the behaviour of G is investigated when both d and ϵ_2 are changed in a manner which keeps their product constant. The product is set by the parameters selected in panel (a), i.e. $d = 100$ nm and $\epsilon_2 = 12.25$. Increasing ϵ_2 is seen to increase $G(\omega)$. For values above $\epsilon_2 = 21.25$ and the corresponding $d \approx 58$ nm, a further increase in ϵ_2 and decrease in d result in a negligible increase in $G(\omega)$ at $\hbar\omega = 0.8$ eV.

The parametric analysis given in figure 6 demonstrates the complexity of optimizing the graphene-waveguide coupling strength. For the sake of simplicity, we now designate the values of $\epsilon_2 = 21.25$ and $d = 58$ nm as optimal at $\hbar\omega = 0.8$ eV and henceforth refer to the corresponding structure as ‘Optimized’. We will later show how it compares with the SOI structure given in figure 2.

4.1. Electro-absorptive optical modulators

In EAMs, the electrically induced change in the absorption coefficient is used in order to modulate light. Actually, by changing the absorption coefficient the modal propagation length $L_e = 1/k_y^I$ is changed. Obviously, the size of L should be at least several times larger than L_e of the mode propagating in the ‘off’ state of the waveguide. Figure 7(a) shows a schematics of a EAM based on the waveguide coupled with graphene. The position of graphene in the waveguide is chosen depending on the mode’s in-plane electric field distribution, as was explained in previous sections.

The shift of the Fermi level in graphene enables switching between the intra- and inter-band transitions and allows the tuning of the absorption coefficient $\alpha = 2\Delta k_y^I$. The dotted and dashed-dotted lines in figure 7(b) show the real and the imaginary parts of the optical conductivity obtained from the [2] data (the one being plotted in figure 1) by displacing both $\sigma^R(\omega)$ and $\sigma^I(\omega)$ so that $2E_F$ falls to 0.8 eV. Such an extrapolation procedure is used for obtaining datasets of $\sigma(\omega)$ for all the values of E_F considered below (other than $E_F = 0.29$ eV, which represents the original dataset). In the absence of experimental data on $\sigma(\omega)$ for varying E_F , this dataset is referred to as experimental. The purpose of considering this ‘artificial’ dataset is to have as realistic data as possible. For comparison, the theoretical $\sigma(\omega)$ curves, obtained using equations (1) and (2) at $E_F = 0.4$ eV, are plotted with full and dashed lines.

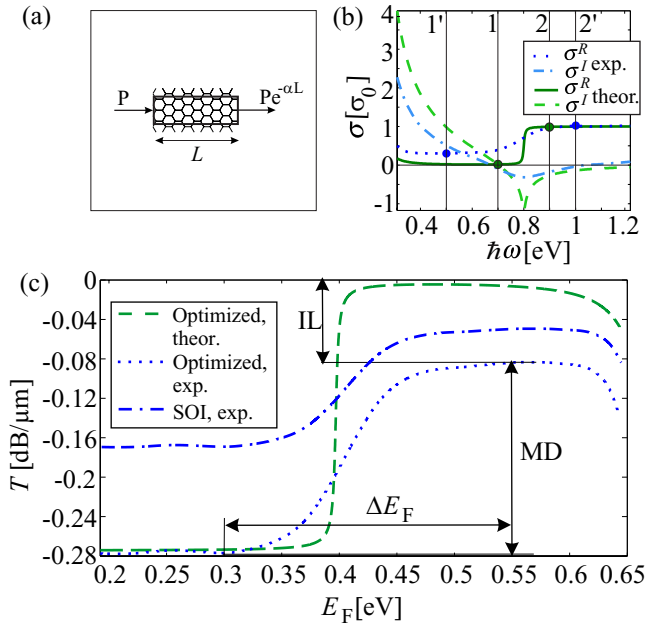


Figure 7. (a) Schematics of a graphene-based EAM. (b) The experimental (dotted and dashed–dotted lines) and theoretical (full and dashed lines) $\sigma(\omega)$ spectra. The vertical lines show the position of 1, 1', 2 and 2' points used to explain the operational principle. (c) The waveguide transmittance in $\text{dB}/\mu\text{m}$ as a function of E_F , calculated for the ‘Optimized’ structure (see section 4) and for the SOI structure in figure 2. The definition of IL, MD and ΔE_F is illustrated for the dotted curve.

The points 1 and 2 (1' and 2') shown in figure 7(b) illustrate how the values of the real part of the conductivity should be chosen in order to achieve a desirable difference between absorption coefficients. The 1 and 1' points correspond to σ^R closest to $2E_F$, for which the absorption coefficient has the lowest value. Similarly, the 2 and 2' points correspond to σ^R closest to $2E_F$, for which the absorption coefficient has the highest value. Clearly, points 1' and 2' are moved further away from $2E_F$ than those of the calculated conductivity, since the slope of the experimental curve is wider than that of the calculated one.

The modulation is achieved by shifting the Fermi level in graphene so that the points 1 (1') and 2 (2') alternately match the operating frequency. The transmission coefficient of the above-described EAM can be calculated as $T_r = \exp(-\alpha L)$. Expressed in $\text{dB}/\mu\text{m}$, the transmission coefficient is given by

$$T_r = \frac{10}{\ln(10)} \times (-2\sigma^R G). \quad (9)$$

Figure 7(c) shows the transmission coefficient calculated from equation (9) versus the position of the Fermi level in graphene. The modulator is operated using the fundamental TE mode at $\hbar\omega = 0.8\text{ eV}$. The dashed line corresponds to the transmission coefficient of a modulator based on the ‘Optimized’ structure from the previous section calculated for the theoretical $\sigma(\omega)$.

In contrast, the dotted line represents T_r of a modulator also based on the ‘Optimized’ structure, but now the experimental dataset of $\sigma(\omega)$ is used. Finally, the dashed–dotted curve

shows the T_r values corresponding to the SOI structure from figure 2 calculated with the experimental $\sigma(\omega)$.

The two key quantities describing a modulator are the MD and the ILs. The MD is defined as the ratio of the maximal and minimal value of the transmission coefficient expressed in $\text{dB}/\mu\text{m}$, as shown in figure 7(c). ILs are defined as the ratio of the maximal value transmission of the bare waveguide and the graphene-coupled waveguide. Since the bare waveguide is assumed to be lossless, the maximal T_r in the former case is equal to $0\text{ dB}/\mu\text{m}$. A comparison of the two curves, which are obtained for the same G and for two different conductivities (dashed and dotted lines in figure 7(c)), shows how the conductivity affects the overall optical performance of EAMs. In the idealized case, σ calculated from equations (1) and (2), $\text{IL} \approx 0.005\text{ dB}/\mu\text{m}$ and $\text{MD} \approx 0.274\text{ dB}/\mu\text{m}$. In the more realistic case, corresponding to the experimental dataset, $\text{IL} \approx 0.082\text{ dB}/\mu\text{m}$ and $\text{MD} \approx 0.196\text{ dB}/\mu\text{m}$. IL is determined by the minimal σ^R belonging to the intra-band region, hence it is smaller in the ideal case. The ratio of maximal σ^R , belonging to the inter-band region, and the minimal σ^R , belonging to the intra-band region, is a good indicator of how high MD would be. On the other hand, the imaginary part of the conductivity determines the phase shift of the propagating wave. Ultimately, the frequency dependence of σ^I could lead to a distortion of the propagating signal with a finite spectral width. The perturbation approach is suitable for analysis of such parasitic effects, since the phase shift could be determined using equation (8). The shift of the Fermi level needed to switch between the states of the maximum and the minimum transmission is $\Delta E_F = 0.1\text{ eV}$ in the ideal case, whereas in the other case $\Delta E_F = 0.25\text{ eV}$. This clearly demonstrates the extent to which the optical performances of EAMs can vary depending on the quality of graphene samples. We also note that $\text{MD} \approx 0.12\text{ dB}/\mu\text{m}$, corresponding to the SOI modulator in figure 7(c), is in reasonable agreement with values of around $0.1\text{ dB}/\mu\text{m}$ reported in [10]. A slightly higher MD of $0.16\text{ dB}/\mu\text{m}$ was experimentally demonstrated for a modulator having two graphene layers [11].

4.2. Electro-refractive optical modulators

ERMs are commonly constructed using Mach–Zehnder interferometers [24–26]. Two waveguides, which are also called the arms, have different real parts of the modal index and this induces a phase lag between the two propagating waves. At the output of the device, where the waveguides are coupled, the waves can interfere constructively or destructively. Figure 8(a) shows a sketch of a Mach–Zehnder modulator based on waveguides coupled with graphene. The waveguides forming the arms are assumed to be the same.

At a given operating frequency, the waves passing through the two arms will interfere constructively or destructively if their relative phase difference, $\Delta\phi$, is $2m\pi$ or $(1 + 2m)\pi$, respectively, where m is an integer. Assuming the length of both arms is set to L , $\Delta\phi = (k_{y,1}^R - k_{y,2}^R)L$, where $k_{y,1}^R$ and $k_{y,2}^R$ are the real parts of the propagation constant in the two arms. Using equation (8), we have

$$\Delta\phi = (\sigma_1^I - \sigma_2^I) GL = \Delta\sigma^I GL. \quad (10)$$

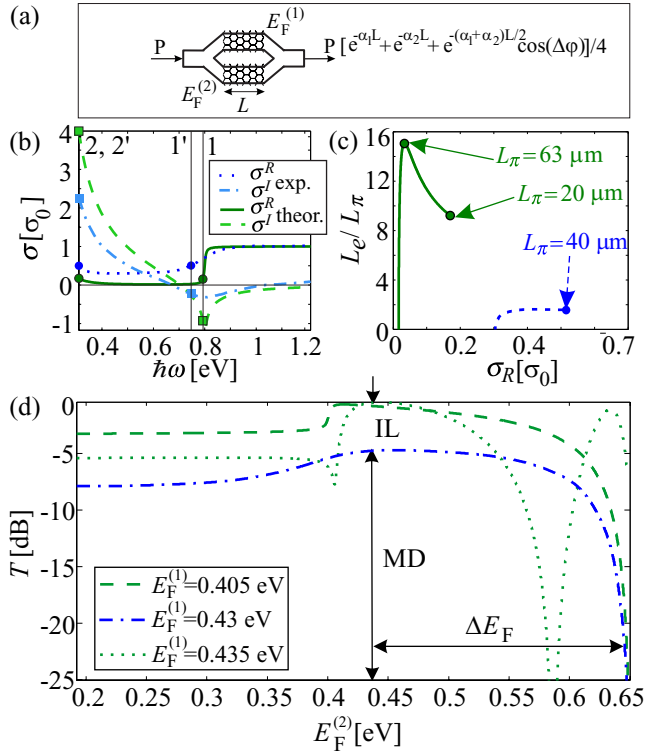


Figure 8. (a) Schematics of a graphene-based ERM. (b) Explanation of the ERM working principle using the experimental (dotted and dashed-dotted lines) and theoretical (full and dashed lines) $\sigma(\omega)$ spectra. The vertical lines show the position of 1, 1', 2 and 2' points used to explain the operational principle. (c) The L_e/L_π ratio versus σ^R , for theoretical (solid line) and experimental (dashed line) conductivities, for the 'Optimized' structure from section 4. (d) Corresponding transmission coefficient versus E_F , calculated for L_π values which are displayed in (c). The definition of IL, MD and ΔE_F is illustrated for the dashed-dotted curve.

Having a higher difference of σ^I in the two arms obviously allows the construction of a shorter modulator. Also, by optimizing the parameters of the waveguide, i.e. by increasing G , the L can be reduced even more. The real part of the conductivity is also important since it determines the absorption of the modes in arms. The absorption should be approximately equal in both arms, in order to allow for a destructive interference (the 'off' state). In the design of an ERM, two characteristic lengths should be considered. The first is the modal propagation length L_e , which we mentioned before and which is given by $L_e = 1/(\sigma^R G)$. The second important length is the length required to achieve a phase shift of $\Delta\phi = \pi$ between the two arms. Using equation (10), L_π it is given by

$$L_\pi = \frac{\pi}{\Delta\sigma^I G}. \quad (11)$$

The $L_e > L_\pi$ condition ensures that the waves are not considerably absorbed before they interfere. This condition is fulfilled if $\Delta\sigma^I > \pi\sigma^R$. Thus, the values of σ^I and σ^R should be chosen in the region below $2E_F$, as is shown in figure 8(b) by points 1, 2, 1' and 2'. Dotted and dashed-dotted lines represent σ^R and σ^I of the experimental dataset, respectively, while the full and dashed lines are the calculated values at $E_F = 0.4$ eV.

Finding the convenient values of $\Delta\sigma^I$ and σ^R is done by looking at the $L_e/L_\pi = \Delta\sigma^I/\pi\sigma^R$ ratio. The idea is to choose a value of $\sigma_{2(2')}^R$ and find the corresponding $\sigma_{1(1')}^I$. The absorption in both arms must be equal, i.e. $\sigma_{1(1')}^R = \sigma_{2(2')}^R$. So the $\sigma_{1(1')}^I$ is automatically determined. Then for a chosen span of $\sigma_{2(2')}^R$ the L_e/L_π is calculated and plotted versus $\sigma_{1(1')}^R = \sigma_{2(2')}^R = \sigma^R$. Figure 8(c) shows such plots. The initial value of $\sigma_{2(2')}^R$ corresponds to a minimal value for which its counterpart $\sigma_{1(1')}^R$ exist. Zeros of the curves in the inset correspond to the initial values of conductivity. The $L_e > L_\pi$ condition is satisfied when the ratio of the two lengths is higher than one. When the theoretical conductivity is used the L_e/L_π curve (solid line) has a distinct maximum of about 15. This is not the case for the other curve (dashed line), calculated using the experimental $\sigma(\omega)$ dataset. For the 'Optimized' structure (see section 4) at $\hbar\omega = 0.8$ eV, L_π corresponding to the L_e/L_π curve maximum is around 63 μm . However, the smallest values of the L_π are obtained for σ^R and σ^I related to the end points of the L_e/L_π curves, as shown in figure 8(c). At those points, the $L_e > L_\pi$ condition is fulfilled and values of L_π are respectively 20 μm and 40 μm . Thus, they represent optimal values.

The modulation of the light is achieved by changing E_F in one of the arms, while it is kept fixed in the other (reference) arm. Here, E_F in the reference arm is denoted by $E_F^{(1)}$ and adjusted to provide matching between the position of point 1(1') and the mode's operational frequency. When the Fermi level in the other arm, denoted as $E_F^{(2)}$, is at the same value as $E_F^{(1)}$, the waves interfere constructively at the output. In contrast, when the $E_F^{(2)}$ is shifted so that the position of point 2(2') matches the operational frequency, the waves interfere destructively at the output. The transmission coefficient of the above-described ERM, in [dB], can be expressed as

$$T_r = 10 \log_{10} \frac{1}{4} \left[e^{-2\sigma_1^R G L} + e^{-2\sigma_2^R G L} + 2e^{-(\sigma_1^R + \sigma_2^R) G L} \cos((\sigma_1^I - \sigma_2^I) G L) \right]. \quad (12)$$

Figure 8(d) shows the transmission coefficient calculated from equation (12) versus the position of the Fermi level in graphene in arm 2. The modulator operates using the fundamental TE mode at $\hbar\omega = 0.8$ eV and is based on the 'Optimized' parameters. The dashed and dotted curves correspond to the theoretical $\sigma(\omega)$ calculated for two different values of the Fermi energy in the reference arm, $E_F^{(1)} = 0.405$ eV and $E_F^{(1)} = 0.435$ eV with corresponding $L_\pi = 20$ μm and $L_\pi = 63$ μm , respectively. The dashed-dotted curve is obtained using the experimental dataset with $E_F^{(1)} = 0.43$ eV and the corresponding $L_\pi = 40$ μm .

The MD and the IL are defined as in the case of EAMs. Since the absorption is held the same in both arms and the length of the arms is chosen to be $L = L_\pi$, the transmission coefficient given by equation (12) is equal to $-\infty$ dB when the waves interfere destructively. Graphs in figure 8(d) are shown starting from $T_r = -25$ dB. Accordingly, the modulation depth is $\text{MD} = \infty$ dB. If the absorption is not the same in the two arms, or if the π phase shift cannot be achieved for

a reasonable L_π , the MD would have a finite value. On the other hand, IL is determined by the real part of σ and has finite values and is smaller when the theoretical $\sigma(\omega)$ is used. The actual values are $IL \approx 0.48$ dB for the theoretical $\sigma(\omega)$ and $IL \approx 4.8$ dB for the experimental dataset. The shift of the Fermi level needed to switch between the states of the maximal and the minimal transmission is $\Delta E_F = 0.245$ eV in the case of $L = 20 \mu\text{m}$ long modulator, and $\Delta E_F = 0.225$ eV in the case of $L = 40 \mu\text{m}$ long modulator (see figure 8(d)). For a longer modulator, the transmission curve has two maxima, as can be seen in figure 8(d). Thus, ΔE_F corresponding to the closer maximum is around 0.065 eV.

The difference between the modulator properties calculated with theoretical and experimental $\sigma(\omega)$ is mainly manifested as a difference in IL and ΔE_F . It is also seen that the minimal modulator length for theoretical $\sigma(\omega)$ is around two times shorter than the one estimated with the experimental dataset.

5. Summary

Optical waveguides incorporating graphene as the electro-optical element are a promising platform for future electro-optical modulators. Their operational principle is based on tuning the optical conductivity $\sigma(\omega)$ of graphene by the application of a gate voltage, thus changing the modal propagation constants k_y .

Here we have described a perturbation method for calculating Δk_y , the graphene-induced change in k_y , from which the quantities such as the modulation depth or insertion losses are directly obtained. On the planar waveguide toy model with realistic material parameters, the method has been shown to possess an excellent accuracy with relative errors in Δk_y of around 1% for the practically relevant cases. It has thus been established that Δk_y is given by the product of a factor characterizing the modal properties of the bare waveguide (the G -factor) and the optical conductivity of graphene. This result has then been used for discussing the optimization of the G -factor and the design principles of both electro-absorptive and electro-refractive graphene-based electro-optical modulators.

Considering that $\sigma(\omega)$ can vary significantly depending on the graphene fabrication procedure and environment, we have simultaneously investigated the predictions of the theoretical and experimental datasets. As expected, the theoretical dataset has been found to predict a considerably better modulator performance. More importantly, however, we have shown that the changes in device performance due to variations of $\sigma(\omega)$ are easily and accurately estimated using the perturbation method.

Acknowledgments

This work was funded by the Serbian Ministry of Education, Science and Technological Development under Project Nos OI171005 and III45018. The authors are also grateful for support by the European Community's 7th Framework Programme under Grant Agreement No 228637 NIMNIL.

References

- [1] Novoselov K S, Geim A K, Morozov S V, Jiang D, Zhang Y, Dubonos S V, Grigorieva I V and Firsov A A 2004 *Science* **306** 666
- [2] Li Z Q, Henriksen E A, Jiang Z, Hao Z, Martin M C, Kim P, Stormer H L and Basov D N 2008 *Nature Phys.* **4** 532
- [3] Nair R R, Blake P, Grigorenko A N, Novoselov K S, Booth T J, Stauber T, Peres N M R and Geim A K 2008 *Science* **320** 1308
- [4] Ando T, Zheng Y and Suzuura H 2002 *J. Phys. Soc. Japan* **71** 1318
- [5] Geim A K and Novoselov K S 2007 *Nature Mater.* **6** 183
- [6] Bonaccorso F, Sun Z, Hasan T and Ferrari A C 2010 *Nature Photon.* **4** 611
- [7] Bao Q and Loh K P 2012 *ACS Nano* **6** 3677
- [8] Xia F, Mueller T, Lin Y, Valdes-Garcia A and Avouris P 2009 *Nature Nanotechnol.* **4** 839
- [9] Mueller T, Xia F and Avouris P 2010 *Nature Photon.* **4** 297
- [10] Liu M, Yin X, Ulin-Avila E, Geng B, Zentgraf T, Ju L, Wang F and Zhang X 2011 *Nature* **474** 64
- [11] Liu M, Yin, X and Zhang X 2012 *Nano Lett.* **12** 1482
- [12] Bao Q, Zhang H, Wang B, Ni Z, Lim C H Y X, Wang Y, Tang D Y and Loh K P 2011 *Nature Photon.* **5** 411
- [13] Jin T K and Choon-Gi C 2012 *Opt. Express* **20** 3556
- [14] Vasic B, Isic G and Gajic R 2013 *J. Appl. Phys.* **113** 013110
- [15] Sun Z, Hasan T, Torrisi F, Popa D, Privitera G, Wang F, Bonaccorso F, Basko D M and Ferrari A C 2010 *ACS Nano* **4** 803
- [16] Koester S J and Li M 2012 *Appl. Phys. Lett.* **100** 171107
- [17] Koester S J, Li H and Li M 2012 *Opt. Express* **20** 20330
- [18] Koester S J and Li M 2014 *IEEE J. Sel. Top. Quantum Electron.* **20** 6000211
- [19] Gosciniaik J and Tan D T H 2013 *Sci. Rep.* **3** 1
- [20] Gosciniaik J and Tan D T H 2013 *Nanotechnology* **24** 185202
- [21] Kim K, Choi J-Y, Kim T, Cho S-H and Chung H-J 2011 *Nature* **479** 338
- [22] Li H, Anugrah Y, Koester S J and Li M 2012 *Appl. Phys. Lett.* **101** 111110
- [23] Cheng Z, Tsang H K, Wang X, Xu K and Xu J 2014 *IEEE J. Sel. Top. Quantum Electron.* **20** 4400106
- [24] Xu C, Jin Y, Yang L, Yang J and Jiang X 2012 *Opt. Express* **20** 22398
- [25] Hao R, Du W, Chen H, Jin X, Yang L and Li E 2013 *Appl. Phys. Lett.* **10** 061116
- [26] Liu A, Jones R, Liao L, Samara-Rubio D, Rubin D, Cohen O N R and Paniccia M 2004 *Nature* **427** 615
- [27] Reed G T, Mashanovich G, Gardes F Y and Thomson D J 2010 *Nature Photon.* **4** 518
- [28] Harrington R F 2001 *Time Harmonic Electromagnetic fields* 2nd edn (New York: Wiley) p 317
- [29] Isic G, Gajic R and Vukovic S 2014 *Phys. Rev. B* **89** 165427
- [30] Palik E D 1998 *Handbook of Optical Constants of Solids* (New York: Academic) pp 555, 753
- [31] Hanson G W 2008 *J. Appl. Phys.* **103** 064302
- [32] Yan H, Xia F, Zhu W, Freitag M, Dimitrakopoulos C, Bol A A, Tulevski G and Avouris P 2011 *ACS Nano* **5** 9854
- [33] Horng J et al 2011 *Phys. Rev. B* **83** 165113
- [34] Jackson J D 1999 *Classical Electrodynamics* (New York: Wiley) p 352
- [35] Anemogiannis E, Glytsis E N and Gaylord T K 1999 *J. Lightwave Technol.* **17** 929
- [36] Zia R, Selker M D, Catrysse P B and Brongersma M L 2004 *J. Opt. Soc. Am. A* **21** 2442
- [37] Landau L D, Lifshitz E M and Pitaevskii L P 2008 *Electrodynamics of Continuous Media* 2nd edn (Amsterdam: Elsevier) p 272
- [38] Martinez A et al 2010 *Nano Lett.* **10** 1506